Design of Interaction Region for a BaF EDM Search

Author:Kang Yuzheng
Supervisors: Klaus Jungmann, Lorenz Willmann
July 06, 2018

A thesis submitted in fulfillment of the requirements for the degree of Bachelor of Physics
at the
University of Groningen

Acknowledgements

I would like to express my deep gratitude to Klaus Jungmann and Lorenz Willmann, my research supervisors, for their patient guidance, enthusiastic encouragement. They really changed my mind on experimental physics. Klaus led me into the field and always help me with the practical issues of my experiment. I like the way how Lorenz presents me the solution when I asked him a question. It not only solved my problem, but also gave a clear mind and structure for my work. Moreover, Thomas Meijknecht, Leo Huisman, and Oliver Böll provided me a lot of supports during my project.

另外，跪谢我的女朋友、准未婚妻、未来的妻子王培每日为我提供了FACETIME充电服务，以及周末影院活动（泪目）。请凭此文换取_____（请自行选填），以对你的各种服务的鼓励表彰！（鼓掌！）以后工资都交给你，六百都不要了。

Kang Yuzheng, 06 July 2018

Abstract

The search for a permanent electric dipole moment requires a state-of-the-art of an interaction zone, where polarized BaF molecules are exposed to parallel an anti-parallel electric and magnetic fields. This thesis presents a steady on magnetic field compensation for an interaction zone. Compensation to a residual was achieved with a low magnetic field (< 2nT) by using set of 3 independent compensation coils and a single layer demagnetized μ metal shell in a $1.6 \cdot 12 \cdot \pi^2 cm^3$ cylinder. Following the application of an external magnetic field on a shielding cylinder, we observed that the magnetization has a relaxation time which dependents on the frequency after externally applied field. With a high magnetic field up to 7.5A/m, the demagnetization in either axial or transverse direction of a cylinder has led to comparable compensation.

Contents

List of Figures

1 Introduction

Since prehistoric times, people have been asking: What is the fundamental law of the universe? By introducing classical mechanics and electrodynamics, mankind could well defined the motion of the macroscopic world. However, scientists never stop pursing the beauty and the unity of the universe. The redundant formula and the clash between the classical picture of a force and the theory of special relativity would not satisfy their desires. The development of the Standard Model merged three(electromagnetic, strong nuclear and weak nuclear force) of four fundamental forces, as well as classifying all known elementary particles[23]. Although the Standard Model gave a fabulous predication on an unknown particle which experimentally found in 2012 named Higgs boson[1], the unconformity with the gravitational force and the evidence of dark matter and dark energy[10] will lead scientific community to verify the most basic laws of nature, and then to search for deviations from them. To this end, high resolution spectroscopy experiments have made crucial contributions over decades. Precision atomic and molecular spectroscopy experiments have been designed to search for simultaneous parity and time-reversal symmetry violation which would manifest themselves on permanent electric dipole moments(EDMs)[6][22].

The existence of permanent electric dipole moment is related to the violation of the charge parity invariance. The theoretical predictions of the permanent electron electric dipole moment(eEDM) is listed in Table:1.1 for various presently theoretical models beyond the Standard Model.

The experimental upper limits on the value of the electron electric dipole moment exhibits different size in different molecules[19].An experiment to search for an eEDM in the barium monofluoride (BaF) molecules is designed to be sensitive to an eEDM value of $d_e = 5 \cdot 10^{-30} e \cdot cm$ and $\epsilon_{eff} = 6 - 8.5 GV/cm$. The enhancement of an eEDM which can be characterized by ϵ_{eff}. This is expected to have an improvement compared to ongoing experiments with YbF and ThO molecules($d_e = 10^{-27} and\ 8 \cdot 10^{-29} e \cdot cm$ respectively)[2][20]. Many groups are searching for an eEDM at this time using different probe molecules. A group at Imperical college is working with YbF, for which the asymptotic value of ϵ_{eff} is 26 GV/cm [15]. A group at Yale university uses PbO molecules with $\epsilon_{eff} \approx 25\ GV/cm$[17].

Table 1.1 – Theoretical predictions for a permanent electric dipole moment on the electron. Current data were extracting from reference [11]

CP Violating Model	$\lvert d_e \rvert \quad [e \cdot cm]$
Standard Model	$\lvert d_e \rvert < 10^{-38}$
Super symmetric models	$\lvert d_e \rvert < 10^{-27}$
Left-right symmetric models	$10^{-28} < \lvert d_e \rvert < 10^{-26}$
Higgs models	$10^{-28} < \lvert d_e \rvert < 3 \cdot 10^{-27}$
Lepton flavor changing models	$10^{-29} < \lvert d_e \rvert < 10^{-26}$

Beyond molecular spectroscopy in the BaF experiment, a controllable magnetic environment is critical aspect of permanent electric dipole moments experiment. In practice, the earth magnetic field and human activities continuously contribute to the field at micro Tesla range with rather large fluctuations[4]. Based on the predictions for a potential signal, the magnetic field inside the molecular interaction zone can be not larger than pico Tesla range in all directions[31]. To achieve 10^7 order of magnitude cancellation of environmental magnetic fields, magnetic shielding and compensation field need to be embedded in the system. The following chapters will deliver conceptual and experimental workouts with practical result achieved nano Tesla range within an interaction zone with a single layer μ-metal shield and electromagnetism coil field compensation. This is a first step towards a multi-layers μ-metal shield, for which the experiment needs later to be achieved.

2 Conceptual framework

2.1 Magnetic shielding

2.1.1 Self shielding

The magnetic field shielding can be achieved by means of shields made of a soft magnetic material with high permeability($\mu_r \gg 1$), and sufficient thickness to attenuate the magnetic field in the shielding shell by providing a low reluctance. The shell of magnetic material with good permeability will reduce the flux intensity inside. According to the Maxwell's equations the magnetic flux tends to remain in the magnetic material layer as the magnetic material offers a low-reluctance path. [9] The field distribution around a single-layer cylindrical shield for transverse direction is[32].

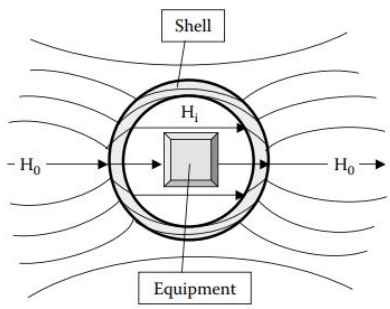

Figure 2.1 – The magnetic shielding with a circular shell in transverse direction. The field lines illustrate the flux density outside, inside and within the shell. The equipment part indicates the interaction zone for EDM experiment.

Multiple hollow cylinders shielding is an essential part of eEDM experiment. With properly shielding, the magnetic field can down to picoTesla range [18]. With 8-layered magnetically shielded room, the Physikalisch Technische Bundesanstalt(PTB) achieved a passive shielding factor at $0.01Hz$ of 75000 and with active shielding over $2 \cdot 10^6$, where shielding factor was

defined as ratio between external field and shielded field.[5] For a single layer, the shielding factor is given by

$$S_{trans} = 1 + \frac{\mu_r t}{2D}, \tag{2.1}$$

where D is cylinder diameter and t is thickness, μ_r is relative permeability[30].

Not only number of shielding layers contribute to the shielding factor, but also the space between the cylinders will also affect the result. It is well know that increasing the separation between two shells improves the shielding performance. For a ideal case, two coaxial infinite long cylinders will give a transverse shielding factor by

$$S_{trans} \approx \frac{\mu_r^2 t^2}{D_1 D_2}(1 - \frac{D_1^2}{D_2^2}), \tag{2.2}$$

where diameters D_1, D_2 satisfied $D_1 > D_2$ [25]. Up to more than two layers, the square ratio term will always dominant and the shielding factor can be approximated by [30]

$$S_{trans} \approx \prod_{i=1}^{n-1} S_{t,n} S_{t,i}(1 - \frac{D_i^2}{D_{i+1}^2}), \tag{2.3}$$

Similar as transverse direction, the axial shielding factor is dominant by the most outer shell. And the theoretical predication is given by

$$S_{axial} \approx \prod_{i=1}^{n-1} S_{a,n} S_{a,i}(1 - \frac{L_i}{L_{i+1}}) \tag{2.4}$$

where L indicates the cylinder length.

Moreover, in most cases, spacing equals to 5% – 10% of the inner shell diameter are wide enough to bring the axial shielding with double-shell closed cylindrical shields to 90% of its maximum. The analytical approximation can be found at [25].

2.1.2 Active shielding

In order to improve the performance of magnetic shielding, one should also consider the active shielding on top of the static shielding or in other term self shielding. Many mature and advanced applications have been used not only within scientific area but also medical area [16]. There are different methods to achieve the active shielding, implementing feedback is

the most optimal one under the majority[7]. The principle behind this is measurement signal feeds into a feedback component which will generate a proper signal to the control coil. With several iterations of this feedback loop, a desired value can be achieved and remain at the preset value. Once the field disturbed, the feedback loop will adjust field again.

In this experiment, the control coil was cubic compensation coil powered by a controllable power supply and the signal from sensor transferred into LabVIEW PID component [12] to adjust the current output for the coil. The optimal configurations of PID controller can be determined by the Ziegler–Nichols method[3][33]. The respond time of the system also contribute to the shielding performance. With a fast respond time, the system can react with fluctuations nearly simultaneous but loose some degrees of precision and vice versa. For a multiple layers shielding case, the cubic compensation coil has less effect on the center of the shielding area due the large shielding factor(more than 3000 if two cylinder shields present[30]). Thus the active shielding by cubic compensation coil becomes less effective, and a new configuration or feedback mechanism should be implemented for a multiple layers active shielding.

2.1.3 Demagnetization

The purpose of demagnetization is to reduce the internal magnetic field of material and provide a zero residual field($\boldsymbol{B} = 0, \boldsymbol{H} = 0$) for further magnetic shielding. In a magnetically linear media(assume to be isotropic) without demagnetization effects,

$$\boldsymbol{B} = \mu \boldsymbol{H} = \mu_0(\boldsymbol{M} + \boldsymbol{H}) \qquad \boldsymbol{M} = \frac{\boldsymbol{B}}{\mu_0} - \boldsymbol{H} = \chi_m \boldsymbol{H} \tag{2.5}$$

, where $\mu_0 = 4\pi \cdot 10^{-7}[N/A^2 or H/m]$ is magnetic permeability of free space, and μ and χ are total linear magnetic permeability and susceptibility respectively. Then

$$\chi_m = \frac{\mu}{\mu_0} - 1 = \mu_r - 1 \tag{2.6}$$

, μ_r defines as relative magnetic permeability. The state of magnetic polarization by the vector quantity is defined by $\boldsymbol{M}$, which is magnetic dipole moment per unit volume. And $\boldsymbol{M}$ is called the magnetization, analogue to the polarization in electric field.[14] In practice, an infinite solenoid(n turns per unit length, current I) is filled with linear material. And this coaxial coil gives

$$\boldsymbol{H} = nI\hat{z} \tag{2.7}$$

. By the application of a decreasing sine wave in current source, the alternating magnetic $\boldsymbol{H}$ field forces the magnetization $\boldsymbol{M}$ on a cyclic passage through the hysteretic loop from saturation point ($\boldsymbol{M}_s$ Figure 2.2) into the demagnetized state and reach the original to achieve a zero field.

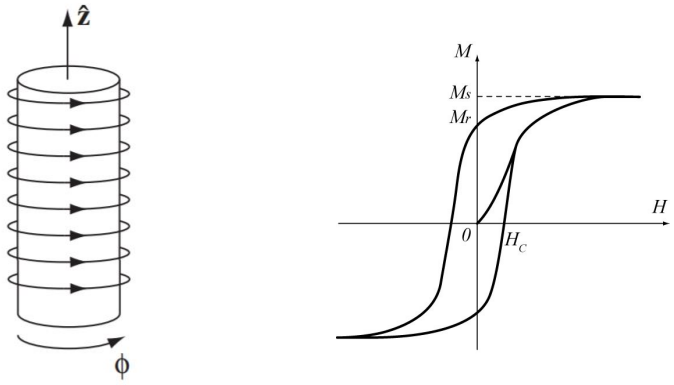

(a) Solenoid coil wound on a cylindrical material

(b) Hysteresis curve of a ferromagnetic material

Figure 2.2 – The figure shows the configuration of coaxial coil with a magnetic field pointing in $\hat{z}$ direction. And the hysteresis curve gives the relation between the external magnetic field and magnetization of a ferromagnetic material. The original point indicates the zero magnetic field.(a) is the coaxial coil wound on a cylinder with the vectors indicate the field direction and coil winding direction. (b) shows the basic concept of hysteresis curve for a ferromagnetic material with saturation magnetization and coercivity labeled on the graph.[8]

Domain wall and Hysteresis curve

Domains are regions of a ferromagnetic material in which the magnetic dipole moments are aligned parallel. When the material is demagnetized the vector summation of all the dipole moments from all the domains equals zero. When the material is magnetized the vector summation of the dipoles gives an overall magnetic dipole. The magnetization process is composed of domain wall displacements[Figure 2.3.a] and rotation of the domain magnetization[Figure 2.3.b].

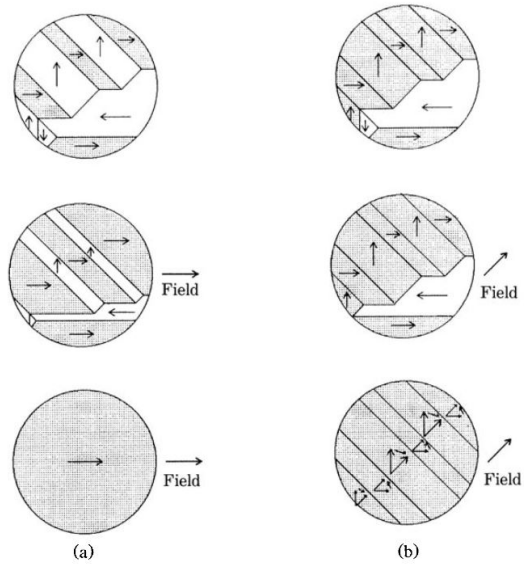

Figure 2.3 – Graphical simulation of displacement(a) and rotation(b) of material domain and domain wall under an external magnetic field. The arrows indicate the magnetization inside material while lines are domain wall of the material[8].

By applying decreasing AC demagnetization, it can realize an isotropic domain distribution(the origin in the following figure).

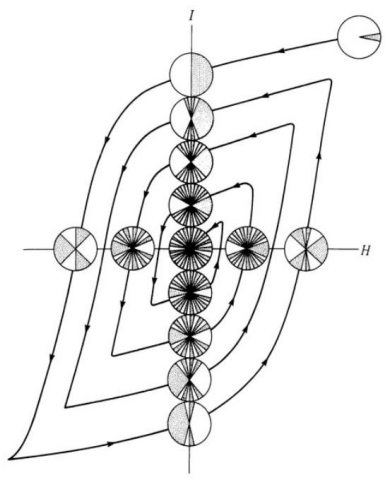

Figure 2.4 – Domain direction and hysteresis curve (grey area indicates the direction of domain)[8].

In general, one can perform demagnetization in arbitrary directions. However, the ferromagnetic material does have a preferable direction. This is due to the immobile domain walls, it can be demagnetized only by rotation of the domain magnetization. If the magnetic anisotropy is uni-axial, and the applied $\boldsymbol{H}$ makes an angle θ_0 with the "easy axis", the domain

magnetization I_s rotates from easy axis towards external field. With different angles, it will behave differently[8].

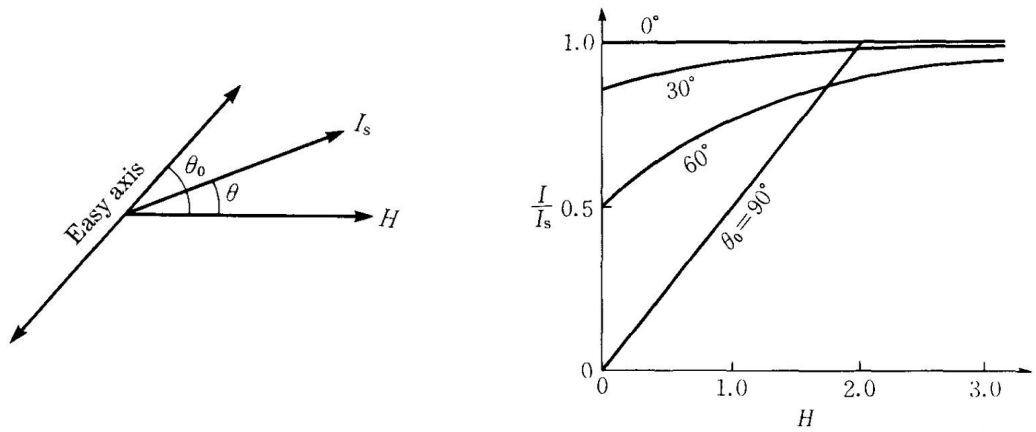

Figure 2.5 – Magnetization curves due to magnetization rotation against the uni axial anisotropy. With left figure indicates the preferable axis of alignment of dipole moment inside material, and external field H, and the rotation of the dipole I_s due to the external field. Right figure illustrates the relation between the external field and intrinsic easy axis inside of a material.[8]

Due to the hysteresis property of ferromagnetic material, applied $\boldsymbol{H}$ field is not linearly correlated to the field $\boldsymbol{B}$ in side material. An analytical result is shown follow.

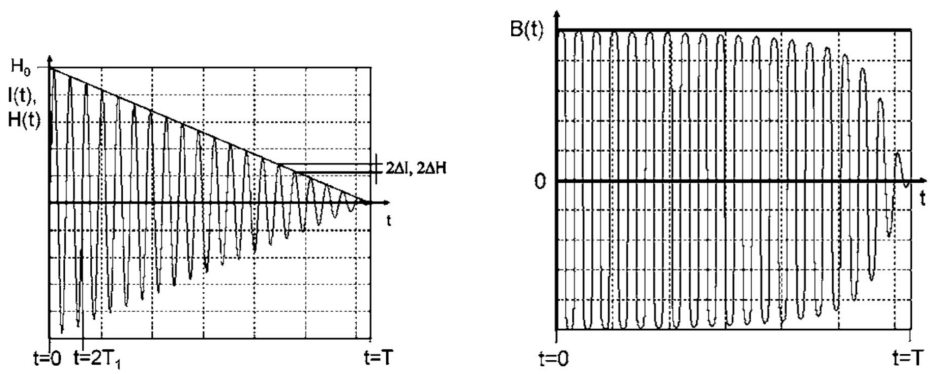

Figure 2.6 – Analytical simulation of an external ramping down sine field and response field inside material. The external field follows linear decrease while the field inside material decrease slowly at the beginning phase. The best values for T are around 5 to 10 minutes with frequency from 10 to 60 Hz[31].

2.1.4 Fields generated by coils

There are variety ways to generate magnetic field in different directions. In this case, three types of coils will introduce to deliver magnetic fields correspond to the cylindrical coordinate.

Firstly set the reference frame at the center of coils with coaxial configuration, the vector pointing along the longitudinal direction as $\hat{z}$, radial vectors pointing perpendicular to the $\hat{z}$ viewed as $\hat{r}$ direction, the circular vectors surround $\hat{z}$ defined as $\hat{\phi}$ direction. David J. Griffiths done all the calculations in his publication, details can found from Introduction to electrodynamics [14].

Field in $\hat{z}$ direction

In this configuration, the demagnetization object(ferromagnetic material) is designed to place at the center of a solenoid. The magnetic field inside solenoid is homogeneous and position independent, the magnitude and direction can be theoretically predict by

$$\boldsymbol{B} = \mu_0 \mu_r n I \hat{z} \tag{2.8}$$

(field inside solenoid).

Field in $\hat{\phi}$ direction

With a toroidal coil, one can generate a $\hat{\phi}$ field with

$$\boldsymbol{B} = \begin{cases} \frac{\mu_0 \mu_r N I}{2\pi r} \hat{\phi} & \text{for points inside the coil,} \\ 0 & \text{for points outside the coil,} \end{cases} \tag{2.9}$$

In order to generate a $\hat{\phi}$ field along the object material, a toroidal coil need to wind on the material itself. This configuration is less flexible and require a complex manufacturing process compared to previous two. The magnetic field generated by this configuration resembles solenoid field.

$$\boldsymbol{B} = \mu_0 \mu_r n I \hat{\phi} \tag{2.10}$$

,(field inside winding area) where n in this case is number of turns per length along the circumference. And the field inside this toroidal field is same as the second case.

3 Experiment

3.1 Principle of measurements

The measurement is the essential part of this experiment. In order to convert physical fields into numerical values, one should minimize all uncertainties that may occur during the experiment and confirm that the observables are indeed what we believed. Therefore, the general principle of the measurement system was in the figure below[Figure: 3.1].

Figure 3.1 – The principle of magnetic field measurement system. The blocks indicate the system devices with arrows show the flow of this system.

Based on the data, we induced the effectiveness of demagnetization and magnetic shielding. We will conclude instrument types and performance characteristics in the following. We will analyze the measurement noise and signal in measurement and result chapter.

The demagnetization measurements were done by same operating sequence which are compensating field, demagnetizing the material, and checking the zero field successively.

3.2 Overview of setup

The experiment system consisted of three parts which are experiment objects(Ferromagnetic metal), control system, and data acquisition system. The setup is shown as follow[Figure: 3.2]. This system can either be controlled manually or automatically using LabVIEW. System can run 7 days times 24 hours. All data were stored simultaneously on a computer with low memory

consumption, which provides a high reliability for long term running measurements. The system was grounded using a thick cable($3 \cdot \pi^2 mm^2$cross section) connected to the grounding ring in the laboratory. The system can operate in different demagnetization functions with maximal output current up to $5A$, and period up to $500s$. The magnetic field generated by demagnetization coil in air cover from Tesla range down to sub nano Tesla range with fine resolution($\sim 0.01nT$, depends on coil, resistors and so on).

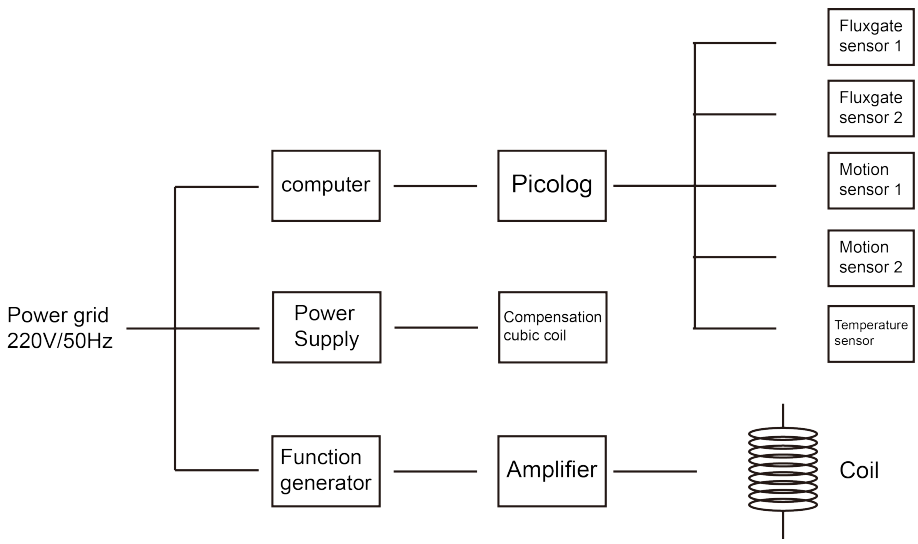

Figure 3.2 – Setup connection configuration. The measurement devices include two fluxgate sensors, two motion sensors, and one temperature sensor. The ADC was used Picolog to convert analog signal to digital values. Controlled devices were programmable power supply and a compensation coil. The demagnetization process was controlled by a function generator and a coil.

The compensation coil brings a controllable background field while multiple environmental sensors provide extra meta data in order to assist data analysis. Measuring shielding factor and demagnetizing sample object are sufficient under this system.

3.3 Cylinders and shielding

In order to avoid stress and tension force on apparatus structure[29], cylindrical shields with uniform thickness and large length-to-diameter ratio were used during the experiment (compared to cubic magnetic shielding rooms). Large scale design has been simulated by COMSOL with different spacing and number of layers to verify feasibility. The experiment cylinders were constructed by weld the edges of one piece of μ-metal plate to form a cylindrical shape. They are considered perfect symmetrical objects. This material is a ferromagnetic alloy with high permeability (relative permeability $0.3 \sim 1 \cdot 10^5$). It has low magnetic anisotropy and magnetostriction, giving it a low magnetic coercivity, which is a crucial parameter in demagnetization process. Therefore μ-metal is commonly used for magnetic shielding.

Table 3.1 – The experimental cylinders with geometric dimensions and field configurations

name	inner diameter cm	thickness mm	long cm	coil type	turns N	field Direction
μ metal 1	6.6	1.0	21.1	-	-	-
μ metal 2	6.0	1.0	13.0	toroidal	40	$\hat{\phi}$
μ metal 3	3.2	1.0	12.0	coaxial	100	$\hat{z}$
μ metal 3	3.2	1.0	12.0	toroidal	15	$\hat{\phi}$
coil 1	6.1	-	15	coaxial	72	$\hat{z}$
coil 2	12	-	40	coaxial	285	$\hat{z}$
coil 3	12	-	40	toroidal	50	$\hat{\phi}$

Three μ-metal cylinders with different dimension were used in this experiment. Two of them were embedded with either toroidal or coaxial coil on themselves giving magnetic field in $\hat{\phi}$ direction and $\hat{z}$ direction. Moreover, three kinds of independent coils were used during the experiment, which can generate field in $\hat{\phi}$ and $\hat{z}$directions. Each of them wound around a tube to provide a solid structure. Because one can easily remove the coil after the demagnetization, this can provide more flexibility during the eEDM measurement. The geometric and electronic figures are tabulated below.3.1 The measurement equipment included a Vernier calliper and a high precision multimeter.

Double layers shielding was performed during this experiment with μ metal 2 and 3, the shielding factor calculated by [Equation: 2.2] is 4544. Furthermore, the multiple shielding with 4 layers was used to provide a constant field inside cubic coil in order to analyze the electronic noise from the system.

3.4 Function generator/ Amplifier

The aim of demagnetization is to reduce the internal magnetic field of the shielding material by implementing alternating magnetic field. In practice, this is obtained by the application of an amplitude modulation current through the demagnetization coil. The amplitude modulation signal was first generated from a function generator using AM mode. With a modulating function (ramp down) and carrier function (sine wave), one can generate an envelope function[Equation: 3.1] which linearly decreases by ΔH and reaches zero at the end of demagnetization period. Therefore, the dipole inside of material will orient in random directions, and magnetic field inside of material will equal to zero.

$$H(t) = \begin{cases} h(t)e(t) = H_0 \sin\omega t(-\frac{1}{T}t+1) & 0 \leqslant t \leqslant T \\ 0 & t < 0 \; or \; t > T \end{cases} \quad with \quad \omega = \frac{2\pi}{T_1}, \qquad T = NT \quad (3.1)$$

With function generator DG6162 RIGOL, frequency(ω), amplitude(H_0), and period(T) can be specified [28]. Number of oscillations, and ΔH will covariant with these parameters. The maximal function period is $500s$, thus the performance of demagnetization was also limited by the function generator. A different modulation functions such as exponential decay, reciprocal function and a different carrier function ,for example block wave, can be selected. The performance of demagnetization will behave differently under aforementioned functions[31][13].

After signal was prepared, it was fed into the amplifier to reach the optimal current range. Then it powers the coil to the saturation point(smaller than micro Tesla range for μ metal 1, 2, and 3.) of Mu-metal and oscillating down to zero at the end of the demagnetization sequence. The demagnetization parameters were mainly controlled by the function generator and the current flowing through the circuit was measured using multimeter.

3.5 Fluxgate

All fields measurements were done using fluxgate magneto sensor(FLC3-70 Stefan Mayer Instruments). These triaxial fluxgate sensors can provide high sensitivity($< nT$), wide measurement range($\pm 200\mu T$). It has low power consumption. One sensor was placed in the centre of compensation coil (see below) to measure the field change due to the operation of the control system, another was placed on the roof above the first one, in order to give a reference background environment field.

The fluxgate magnetometer consists of a ferromagnetic material wound with two coils, a drive and a sense coil. The drive coil carries an alternating current creating an alternating magnetic field. This field drives the ferromagnetic material inside sensor to reach saturation, and back to zero, then towards opposite direction following the hysteresis curve of the ferromagnetic material. If an external magnetic field is present, the flux through the sensing coil will deviate from original value and induce a voltage with sense coil. The sensor contains electronics parts which can be weakly magnetized and the output signals are temperature dependent according to the manufactured data sheet. However, these uncertainties were below the precision range ($< nT$) of the current device. Thus they can be regarded as higher order perturbations during the measurements.

Two fluxgate sensors were powered by a constant voltage($\pm 5V$) through two power adapters. Moreover, Two low pass filters were connected between power adapters and fluxgate sensors aiming to filter out high frequency signal(feeding current from power supply) [Figure 3.3b]. The cut off frequency is $91Hz$, and response time is 0.01s.

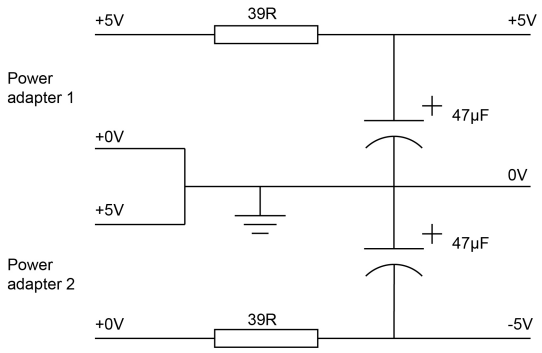

(a) Pass filter circuit

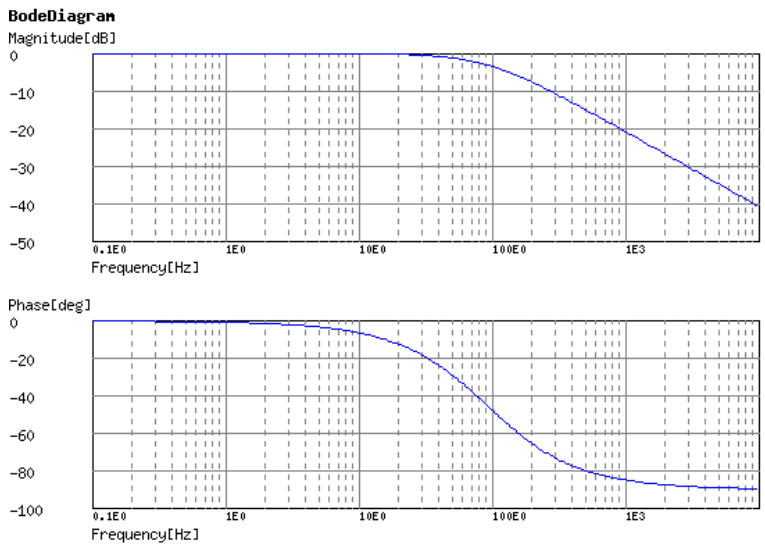

(b) Low pass filter Bode diagram

Figure 3.3 – This figure shows the low pass filter circuit diagram for the power supply of fluxgate sensors. This power supply was able to give $\pm 5V$ and filter out high frequency noise. The bode diagram indicates the frequency dependence of the input power.

With this configuration, the power source can remain constant for a long term experiment with voltage variation less than $0.1V$. Alkaline battery can be used for a short term measurement. After running more than $1 \sim 2$ weeks, it will drain out. Therefore the performance of sensor will differ from the original.

3.6 Picolog

The ADC-24 high-resolution data logger with Terminal Board from Pico technology[27] was used to acquire the signal from the fluxgate sensor[21]. This data logger is designed to measure voltages in the range of ± 2.5 volts with maximal 20 digits. It is powered by the USB connection of the computer readout through a USB cable($5V$, $50Hz$). It is grounded externally to the

building grounding ring. Data acquisition can either be controlled by Picolog software or LabVIEW with the help of the developer package provided by Pico Technology[27]. Differential input configurations were set up to eliminate the common source noise. A temperature and two motion sensors were attached to the Picolog input board in order to acquire metadata. The general configuration is shown below[Figure 3.4]. The cables need to connect tightly, otherwise signals will have interference.

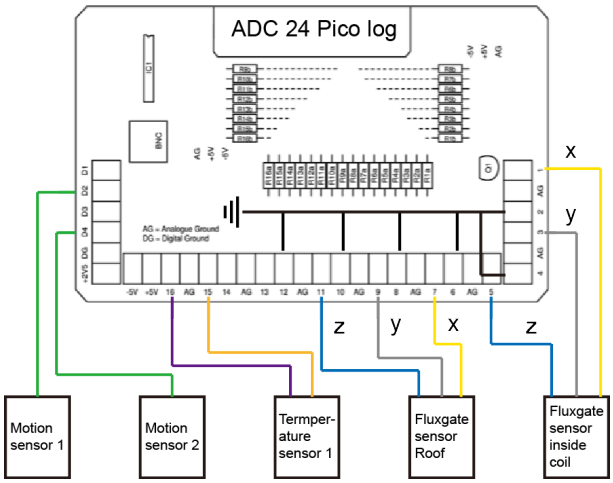

Figure 3.4 – The connection circuit with measurement devices and data logger. The blocks are external devices, and port numbers are shown on the pico log board.

To obtain the best resolution, conversion time 660ms and voltage range $\pm 313mV$ were chosen. With these settings, the data logger has the best noise-free resolution ($5.97 \cdot 10^{-4} mV$). Under the combination ADC24 and FLC3-70, one can perform a sub nano-tesla range field measurement($0.02nT$). Nevertheless, the noises rule out the best sensing resolution which will be analysed in following chapter.

3.7 Compensation coil

The cubic compensation coil was built to compensate large magnetic field ($< 100\mu T$) and provided a controlled environment to verify magnetic shielding and demagnetization. Three coaxial coils were mounted on the edges of a cubic skeleton made by aluminum with dimension $65 * 65 * 65\ cm^3$. The magnetic field can be generated on x,y,z directions independently. One of the fluxgate sensor was placed in the center of the compensation coil and took the measurement data through entire experiment. Object materials were placed on a platform with same height as fluxgate sensor.

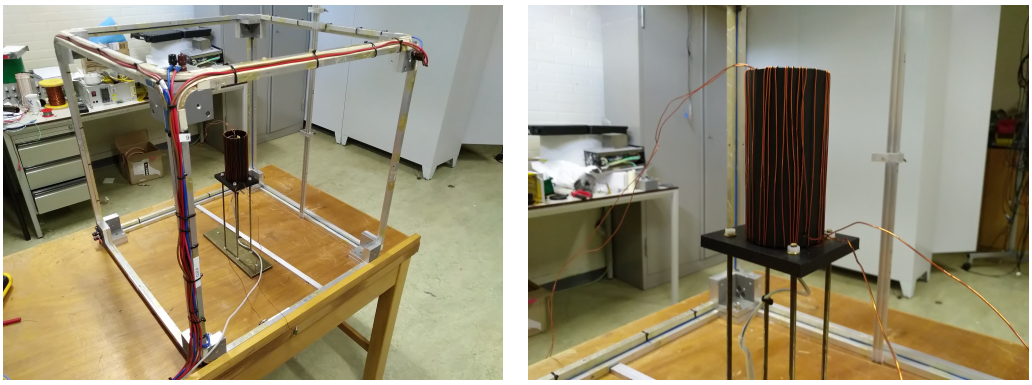

(a) Sample and cubic compensation coil (b) Mu-metal at test position

Figure 3.5 – The experiment setup for magnetic shielding and compensation at KVI.

This compensation coil able to provide a well defined magnetic field on x direction $52.7nT/mA$, y direction $38.8nT/mA$, and z direction $45.4nT/mA$. Based on the simulation result, the central area of the compensation coil can be viewed as a homogeneous field. By control the power supply, one can determine the shielding factor and other properties of test samples.

3.8 Software

The magnetic field measurement is sensitive to the environment. Any unnoticeable human activity could cause a large deviation of the field measurement. Therefore integrating entire system and remote control needed to be considered for a long term wise. Based on the experiment devices, there were multiple options to achieve the remote control and integration. Nevertheless, LabVIEW provides the easiest solution for this case. On the one hand, LabVIEW has maintained by National Instruments over a long time, which provide a stable and programming friendly environment to work with. On the other hand, there are abundant portable devices with mature samples for scientific measurement.

Under this experiment, the Picolog board (ADC-24), programmable power supply(HMP2032, ROHDE&SCHWARZ) and the function generator (RIGOL DG4162) were able to operate by LabVIEW. One can perform shielding factor measurement, negative feed back loop (PID), demagnetization, and active shielding with digital control panels on a computer. Both the programmable power supply and the function generator have LabVIEW drivers, devices were easily controlled by "subvi" block functions in LabVIEW through VISA (Virtual Instrument Software Architecture). Moreover, Pico technology released the PicoSDK which makes the assess through LabVIEW available[27]. The streaming data acquisition follows certain sequence which can be found at Github [26].

4 Data analysis and results

After collecting two months measurement data, raw data need to process in an illustrated format and provide a clear comparison with each configuration. In this chapter, cylinders with different geometric shapes, demagnetization frequencies, demagnetization fields will be compared. And the corresponding shielding factor indicates the effectiveness of demagnetization. Moreover, by implementing the discrete Fourier transformation, the noises from human activity and system will be analysed in a frequency domain. The measurement data were converted into magnetic field dimension[Tesla] with the conversion factor [21]. And zero Volt output indicates no magnetic field passing through the magnetometer.

In the last part, the ability of magnetic shielding will be demonstrated. By the combination of the compensation coil and a proper demagnetized μ-metal shell, a nano Tesla range field can be maintained with fluctuations smaller than 2 nano Tesla over days.

4.1 Demagnetization with different frequencies

The different frequencies affect the oscillation numbers and ramp down internal of the demagnetization modulation function[Equation: 2.5]. Thus the effectiveness of demagnetization were differ from each frequency. During the experiment, the μ metal cylinder [Table: 3.1 μ metal 3] with field direction on $\hat{z}$ was set up. The demagnetization behaviour is shown on figure 4.1.

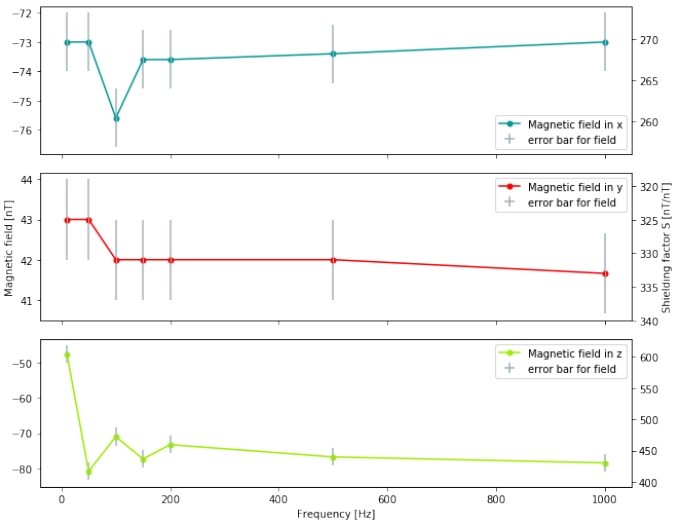

Figure 4.1 – The magnetic fields of a μ metal cylinder with 12cm long, 3.2cm diameter after running demagnetization(300 seconds, maximal current 3A, ramping down sine wave). The magnetic fields before the demagnetization were -223nT, 180nT, -852nT in x, y, and z directions. Shielding factors were calculated base on the ratio between field inside of cylinder and the background field measured by an additional fluxgate sensor.

4.2 Relaxation time with respect to different frequencies

Upon application of an external magnetic field, delayed changes in the magnetization of a μ metal shell was observed. The high frequency oscillation will bring a longer relaxation time than a low frequency signal which can ranging from second to hours. During the experiment, 0.5, 1, 5, 10, 30, 50, 60Hz driving frequencies were implemented to the demagnetization process. In the following, the time versus frequency will be compared. Due the demagnetization has preferable directions as mentioned at Figure 2.5, the direction versus relaxation also shown in the graph.

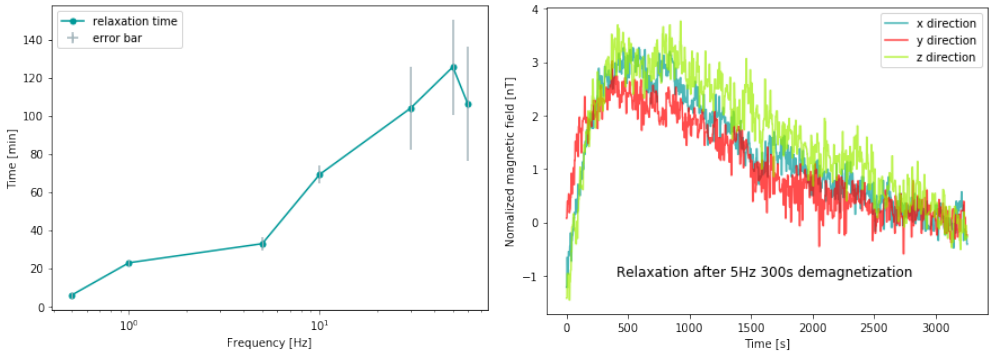

(a) Relaxation time in different frequencies

(b) Relaxation in different directions

Figure 4.2 – The relaxation time measurements after 300s 2A demagnetization with a μ metal cylinder 12cm long, 3.2cm diameter. The high frequency gave a longer relaxation time with a larger uncertainty while different directions under same demagnetization conditions show same behaviour of relaxation. The field changes because of relaxation were smaller than 5nT for all experimental frequencies(0.5, 1, 5, 10, 30, 50, 60Hz).

4.3 Different geometric objects and field coils

It turns out the demagnetization with μ metal 1, 2, 3(Table: 3.1) had a comparable residual field at the end. The geometric shape within 25cm long and 7cm diameter did not play an important role at this stage. The field coils which wound on the μ metal itself had better demagnetization performances than the external coils. Demagnetization in either $\hat{z}$ or $\hat{\phi}$ can reduce the magnetization effectively. The shielding factors in transverse direction for the three cylinders were 159 ± 61, 211 ± 43, and 314 ± 75 which close to the theoretical predictions 227, 250, 500 respectively.

4.4 Noise Analysis

There were two main sources of noise. One was human activity disturbances, the other was systematic noise. By implementing discrete Fourier transformation, it is able to recognize human activities by the specific spectrum. However, with one second sampling time, high frequency signals will hidden among the average. Due to the large amount measurement data, it will reveal the traces in some degrees. For instance, the following figure demonstrate the frequency domain of measurement signals[figure: 4.3b]. By the same time, there was cyclotron accelerator experiment running frequently. The character of this disturbance is easy to recognize, all signals will move to one direction simultaneously.

On the other hand, the measurement system also had contributions to the noise part. It was due to thermal noise, device instability and so on [24]. By measuring signal output without powering sensor devices, one can conclude the white noise of this system.

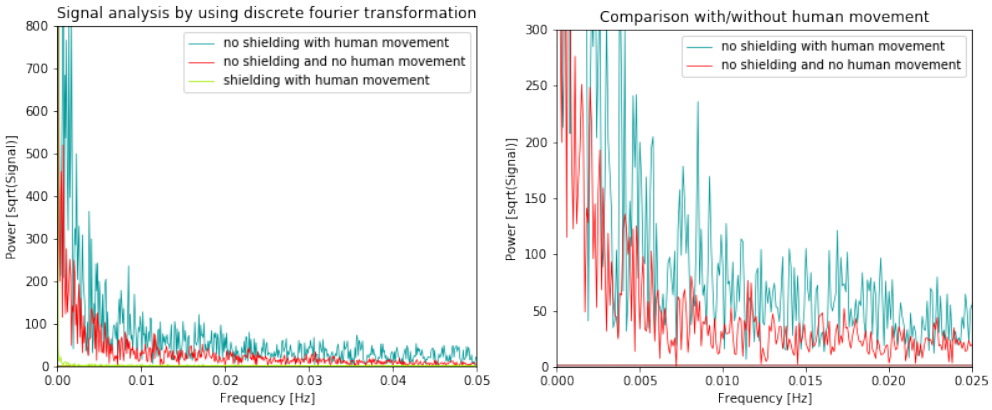

(a) Measurement signal in frequency domain (b) Zoom in view of non-/human activities

Figure 4.3 – Magnetic field measurements in frequency domain with comparison between non-/human activity and shielding. The frequency domain already averaged by the system sampling time 1 second. b part indicates the zoom in view of no shielding signals with frequency range 0 to 0.025Hz and power from 0 to 300. Human activity enlarged signals over entire frequency range, there were several peaks located at 0.005 and 0.007Hz.

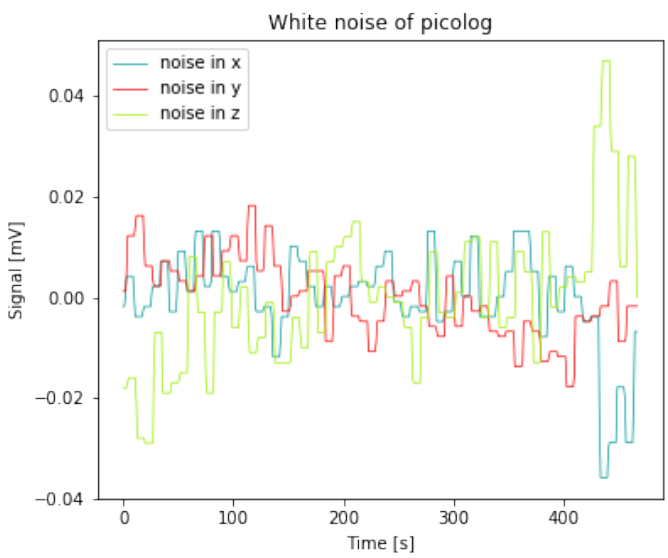

Figure 4.4 – The white noise measurement of Picolog device using same ports of fluxgate sensor. The standard deviations of x, y, z are 0.009, 0.008, and 0.014 mV respectively. And the correspond fluctuations in field measurement were 0.3, 0.28, and 0.5 nT. The conversion time was one second, data were inter connected with straight lines by sacrificing continuity of the data.

4.5 "Zero field"

By the combination of a compensation coil and a one layer of μ metal shell, the magnetic field can be lowered down to nano Tesla range. The procedure were followed with zeroing the field with the compensation coil, putting the demagnetized shell inside of the compensation coil, re-calibrating the magnetic field using the compensation coil successively.

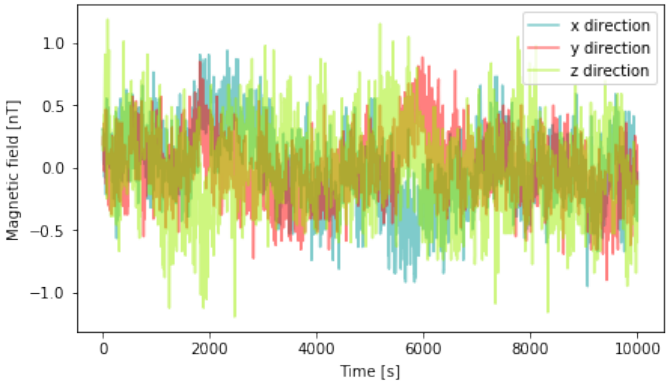

Figure 4.5 – The magnetic field inside interaction zone was maintained by a compensation coil and a demagnetized μ metal shell. This setup could run several days for magnetic fluctuation lower than 2nT. This figure demonstrates the magnetic field data within 3 hours with 0.31nT, 0.26nT, 0.44nT standard deviations in x, y, z directions. The systematic noise was at same range, so the fluctuations were concluded from the system.

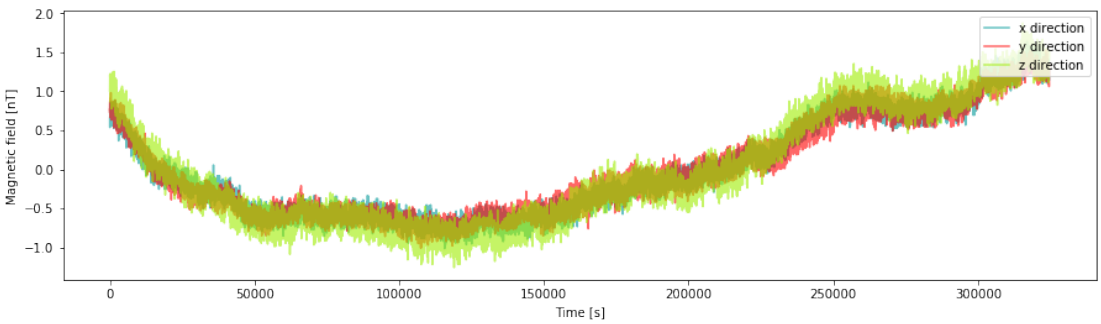

Figure 4.6 – The magnetic field inside interaction zone was maintained by a compensation coil and a demagnetized μ metal shell. This measurement was taken from 8th of June to 11st of June 2018.

5 Discussion and Conclusions

In this chapter, the technique of magnetic shielding and demagnetization will be discussed and concluded. The improvement suggestions of experiment apparatus will be made in the following part.

By implementing one shell μ metal cylinder and a compensation coil, the system was able to maintain the magnetic field within 2 nano Tesla over days and cancel most of magnetic field generated by earth and human activity. The multiple layers shielding also gave a stable magnetic field. Nevertheless, the compensation coil need to place in a proper way in order to zeroing the field for multiple cylinders at the end. The hollow cylinders were able to bring down the magnetic field in axial direction with a shielding factor 140 even without an end cap. Based on the measurement data, the demagnetization using oscillation field worked on the μ metal cylinders. The optimal demagnetization time is around 5 to 10 minutes with oscillation frequency from 10 to 60Hz which can generate 3000 to 36000 turns of each demagnetization period. The $\boldsymbol{H}$ fields generated by experiment coils were around $7.5 A/m$, and sufficient to bring the μ cylinders in either saturation or demagnetization state. Although μ metal has an intrinsic preferable direction of alignment of dipole moment, demagnetization fields acting on either axial or transverse direction can both have expected field at the end.

Moreover, the reading precision and noise from measurement devices limited the opportunity for field measurement into pico Tesla range. With one second sampling time at current configuration, the high frequency signals will average out. In order to perform an accurate data analysis, a fast reading rate with high precision is required. On the other hand, the sampling rate also limited the performance of active shielding in the future.

In general, the magnetic shielding by using multiple μ metal cylinders is able to create an interaction field for later eEDM experiment. By properly implementing shells and compensation field, a low magnetic field interaction zone can be generated with a low variance over a long time.

Bibliography

[1] Georges Aad, Brad Abbott, Jalal Abdallah, S Abdel Khalek, O Abdinov, Rosemarie Aben, Babak Abi, Maris Abolins, OS AbouZeid, Halina Abramowicz, et al. Evidence for the higgs-boson yukawa coupling to tau leptons with the atlas detector. *Journal of high energy physics*, 2015(4):117, 2015.

[2] Parul Aggarwal, Hendrick L Bethlem, Anastasia Borschevsky, Malika Denis, Kevin Esajas, Pi AB Haase, Yongliang Hao, Steven Hoekstra, Klaus Jungmann, Thomas B Meijknecht, et al. Measuring the electric dipole moment of the electron in baf. *arXiv preprint arXiv:1804.10012*, 2018.

[3] Derek P Atherton. Almost six decades in control engineering [historical perspectives]. *IEEE Control Systems*, 34(6):103–110, 2014.

[4] Jeremy Bloxham and David Gubbins. The variation of earth's magnetic field. *Nature*, 317(6040):777, 1985.

[5] J Bork, HD Hahlbohm, R Klein, and A Schnabel. The 8-layered magnetically shielded room of the ptb: Design and construction. In *Biomag2000, Proc. 12th Int. Conf. on Biomagnetism*, pages 970–73. Espoo, Finland, 2001.

[6] FJ Botella, LM Garcia Martin, D Marangotto, F Martinez Vidal, A Merli, N Neri, A Oyanguren, and J Ruiz Vidal. On the search for the electric dipole moment of strange and charm baryons at lhc. *The European Physical Journal C*, 77(3):181, 2017.

[7] Caltech. Control and dynamical systems. http://www.cds.caltech.edu/~murray/books/AM08/pdf/am06-pid_16Sep06.pdf, 2008.

[8] Chikazumi and C. D. Graham. *Physics of Ferromagnetism 2e.* Number Vol. 94 in International Series of Monographs on Physics. OUP Oxford, 1997.

[9] William John Duffin. *Advanced electricity and magnetism for undergraduates.* McGraw-Hill, 1968.

[10] John Ellis. Physics beyond the standard model. *Nuclear Physics A*, 827(1-4):187c–198c, 2009.

[11] Sebastian A. R. Ellis and Gordon L. Kane. Theoretical prediction and impact of fundamental electric dipole moments. *springer*, 2016.

[12] Graham C Goodwin, Stefan F Graebe, and Mario E Salgado. Control system design. *Upper Saddle River*, 13, 2001.

[13] GOUDSMIT. Degauss solution. https://www.goudsmitmagnets.com/industrial-magnetic-systems/demagnetization.(accessed:17.06.2018.

[14] D. J. GRIFFITHS. *Introduction to electrodynamics*. Cambridge University Press; 4 edition, 2017.

[15] JJ Hudson, BE Sauer, MR Tarbutt, and EA Hinds. Measurement of the electron electric dipole moment using ybf molecules. *Physical review letters*, 89(2):023003, 2002.

[16] Peter Jezzard. Shim coil design, limitations and implications. In *International Society of Magnetic Resonance in Medicine (ISMRM) Annual Meeting*, 2006.

[17] David Kawall, F Bay, S Bickman, Y Jiang, and D DeMille. Precision zeeman-stark spectroscopy of the metastable a (1)[σ+ 3] state of pbo. *Physical review letters*, 92(13):133007, 2004.

[18] IK Kominis, TW Kornack, JC Allred, and MV Romalis. A subfemtotesla multichannel atomic magnetometer. *Nature*, 422(6932):596, 2003.

[19] Aaron E Leanhardt, John L Bohn, Huanqian Loh, Patrick Maletinsky, Edmund R Meyer, Laura C Sinclair, Russell P Stutz, and Eric A Cornell. High-resolution spectroscopy on trapped molecular ions in rotating electric fields: A new approach for measuring the electron electric dipole moment. *Journal of Molecular Spectroscopy*, 270(1):1–25, 2011.

[20] J Lim, JR Almond, MA Trigatzis, JA Devlin, NJ Fitch, BE Sauer, MR Tarbutt, and EA Hinds. Ultracold molecules for measuring the electron's electric dipole moment. *arXiv preprint arXiv:1712.02868*, 2017.

[21] Stefan Mayer. Data sheets. https://stefan-mayer.com/en/downloads.html.

[22] Nikhef. The edm program in groningen. https://indico.nikhef.nl/event/60/contribution/2/material/slides/0.pdf.

[23] Robert Oerter. *The theory of almost everything: The standard model, the unsung triumph of modern physics*. Penguin, 2006.

[24] Henry W Ott and Henry W Ott. *Noise reduction techniques in electronic systems*, volume 442. Wiley New York, 1988.

[25] Eugene Paperno, Saee Peliwal, Michael V Romalis, and Anton Plotkin. Optimum shell separation for closed axial cylindrical magnetic shields. *Journal of applied physics*, 97(10):10Q104, 2005.

[26] PicoTech. Pico streaming data. https://github.com/picotech/picosdk-ni-labview-examples.

[27] PicoTech. Picosdk 10.6.12. https://www.picotech.com/downloads/.

[28] RIGOL. Dg4000 series specifications. http://beyondmeasure.rigoltech.com/acton/attachment/1579/f-0168/0/-/-/-/-/file.pdf, 2018.

[29] David Roylance. *MECHANICAL PROPERTIES OF MATERIALS(Lecture notes)*, chapter 1,4,5, pages 5,51,79. MIT, 2008.

[30] TJ Sumner, JM Pendlebury, and KoF Smith. Convectional magnetic shielding. *Journal of Physics D: Applied Physics*, 20(9):1095, 1987.

[31] F. Thiel, A. Schnabel, S. Knappe-Grüneberg, D. Stollfuß, and M. Burghoff. Demagnetization of magnetically shielded rooms. *Review of Scientific Instruments*, 78(3):035106, 2007.

[32] Xingcun Colin Tong. *Advanced materials and design for electromagnetic interference shielding*. CRC press, 2016.

[33] JG Ziegler and NB Nichols. Optimum settings for automatic controllers. *Journal of dynamic systems, measurement, and control*, 115(2B):220–222, 1993.